Euler-Poincaré characteristics of classes of disordered media

C. H. Arns,[1] Mark A. Knackstedt,[1,2,*] W. V. Pinczewski,[1] and K. R. Mecke[3]
[1]*School of Petroleum Engineering, University of New South Wales, Sydney, NSW 2052, Australia*
[2]*Department of Applied Mathematics, Research School of Physical Sciences and Engineering, Australian National University, Canberra ACT 0200, Australia*
[3]*Fachbereich Physik, Bergische Universitat Wuppertal, D-42097, Germany*
(Received 3 July 2000; revised manuscript received 9 November 2000; published 27 February 2001)

We consider a family of statistical measures based on the Euler-Poincaré characteristic of *n*-dimensional space that are sensitive to the morphology of disordered structures. These measures embody information from every order of the correlation function but can be calculated simply by summing over local contributions. We compute the evolution of the measures with density for a range of disordered microstructural models; particle-based models, amorphous microstructures, and cellular and foamlike structures. Analytic results for the particle-based models are given and the computational algorithm verified. Computational results for the different microstructures exhibit a range of qualitative behavior. A length scale is derived based on two-point autocorrelation functions to allow qualitative comparison between the different structures. We compute the morphological parameters for the experimental microstructure of a sandstone sample and compare them to three common stochastic model systems for porous media. None of the statistical models are able to accurately reproduce the morphology of the sandstone.

DOI: 10.1103/PhysRevE.63.031112 PACS number(s): 02.50.−r, 05.40.−a, 47.55.Mh, 81.05.Rm

INTRODUCTION

The structure of a disordered material—an oil bearing rock, a piece of paper, or a polymer composite—is a remarkably incoherent concept. Despite this, scientists and engineers are asked to predict the properties of a disordered material based on the ''structure'' of its constituent components. A major shortcoming in the understanding of processes involving complex materials has been an inability to accurately characterize microstructure. The specification of the structure requires topological as well as geometric descriptors to characterize the connectivity and the shape of the spatial configuration. In oil recovery from petroleum reservoir rocks, an area of particular interest to the authors, recovery depends crucially on the topology of the pore space and on the mean curvature of the surfaces where immiscible phases meet at a contact angle. To determine accurate flow models and to devise intelligent recovery strategies, an accurate characterization of reservoir rocks in terms of topology and geometry is required.

To date, the toolkit used to quantify complex structures has been primarily that of the statistical physicist. Complete characterization of the effective morphology, however, requires knowledge of an infinite set of *n*-point statistical correlation functions. In practice only lower-order morphological information is available; common methods [1] are based on matching the first two moments (volume fraction and two-point correlation function) of the binary phase function to a random model. It is widely recognized that although the two-point correlation function of a reference and a reconstructed system is in good agreement, this does not ensure that the structures of the two systems will match well, and attempts to reconstruct materials from experimentally measured two-point information have not been very successful [2,3]. The same problem has been encountered at the atomic scale in characterizing and comparing amorphous atomic glasses, where two-point correlation functions are recognized to give poor structural signatures. The function is nonunique and does not capture many important features of the microstructure.

Other useful two-point characterizations of microstructure include the chord-length distribution function [4,5] (and the related lineal-path function [6]) and the pore-size distribution function [7]. However reconstructions of experimental data sets based on these characterizations have been shown to give a poor representation of the connectivity of the systems [8]. Functions that may provide more complete information about connectivity [9] are unfortunately too complex to incorporate into reconstruction schemes [8]. Incorporation of three- and four-point information may lead to a better estimation of structure, but their measurement is very complex and it is not clear how to incorporate the information within reconstruction algorithms.

There is a need for morphological measures which include higher-order correlations, but are fast and reliable for characterizing the morphology of a structure. Statistical measures that are sensitive to the morphology of structures have been extensively investigated in other fields such as image analysis and pattern recognition [4,10,11]. Integral geometry provides a suitable family of morphological descriptors, the Minkowski functions (MFs). These measures embody information from every order of the correlation functions, are numerically robust even for small samples, are independent of statistical assumptions on the distribution of phases, and yield global as well as local morphological information. The MFs are additive measures allowing one to calculate these measures effectively by simply summing over local contributions. The measures are based on the Euler-Poincaré char-

*Corresponding author.
Email address: mak110@rsphysse.anu.edu.au

 ©2001 The American Physical Society

acteristic of n-dimensional space. In a d-dimensional space there are $d+1$ such measures. In three dimensions the functionals are related to the familiar measures of volume fraction, surface area, integral mean curvature, and Euler characteristic. These measures are efficiently calculated at the local scale from digital images [12,13]. MFs have been used previously to distinguish quantitatively between different complex morphologies, to characterize turbulent and regular Turing patterns from chemical reaction-diffusion systems [14], to show that the hole distribution in thin films are inconsistent with the concept of spinodal decomposition, but consistent with a nucleation scenario [15], and to discriminate between different cosmological models of the early universe [16]. Measurements of the MFs for model random materials has to date been made on only a simple random filling of a cubic network [17].

In this paper we consider the evolution of the Minkowski functionals for a range of complex morphologies. We loosely consider three types of model microstructures: (1) Particle-based models, models based on Poisson distributed overlapping and nonoverlapping spheroids that generate granular packs, sintered spheroid packs, etc.; (2) Models based on level cuts of Gaussian random fields that describe the morphology of amorphous alloys [18], disordered microemulsion phases [19,20], and polymer composites [21–23]; and (3) models based on Voronoi tesselations of Poisson-distributed points that result in closed-cell and open-cell foams [24] and fibrous bundles. We derive analytic results for Poisson-distributed particles and verify the computational algorithm. The MFs for the range of microstructures are then presented and we discuss the qualitative differences observed. We compute the morphological parameters for the experimental microstructure of a sandstone sample and compare to them three different stochastic model systems. None of the statistical models are able to accurately reproduce the morphology of the sandstone.

The plan of the paper is as follows. In the next section we review concepts in mathematical morphology and give the theoretical predictions for the MFs of Poisson-distributed cubes and spheres. We then describe the computational algorithm, the generation of the model microstructures, and verify the algorithm against theory. In the following section we present numerical predictions of the MFs for a range of microstructures.

I. MINKOWSKI FUNCTIONALS

In this study we consider the Minkowski functionals of digitized representations of complex media at various volume fractions. We consider a two-component medium filling a cubic volume $V=L^d$. A digitized set $\mathcal{Q}=\cup_i Q_i$ of either component can be described by a collection of voxels Q_i or compact (closed and bounded) convex sets. In order to characterize $\mathcal{Q}$ in a morphological way, let us first recall some basic facts from combinatorial integral geometry [25,13]. The convex ring $\mathcal{R}$ constitutes the stage for our model. $\mathcal{R}$ denotes the class of all subsets A of the Euclidean space $\mathbb{R}^d$, which can be represented in terms of a finite union of bounded closed convex sets. Clearly, digitized spatial configurations $\mathcal{Q}$ belong also to the convex ring $\mathcal{R}$.

The Euler characteristic χ is introduced as an additive functional over $\mathcal{R}$, so that for $A,B\in\mathcal{R}$,

$$\chi(A\cup B)=\chi(A)+\chi(B)-\chi(A\cap B) \tag{1.1}$$

and

$$\chi(A)=\begin{cases}1, & \text{convex } A\neq\emptyset\\ 0, & A=\emptyset.\end{cases} \tag{1.2}$$

We note that this functional χ coincides with the Euler-Poincaré characteristic in algebraic topology. The Minkowski functionals over $\mathcal{R}$ are now defined through

$$W_\nu(A)=\int \chi(A\cap E_\nu)\,d\mu(E_\nu). \tag{1.3}$$

Here, E_ν is a ν-dimensional plane in $\mathbb{R}^d$, $d\mu(E_\nu)$ denotes its kinematical density normalized so that for a d-dimensional ball $B_d(r)$ with radius $r, W_\nu(B_d(r))=\omega_d r^{d-\nu}; \omega_d=\pi^{d/2}/\Gamma(1+d/2)$ is the volume of the unit ball. From definition (1.3) it is clear that the Minkowski functionals inherit additivity from χ. For lattice configurations $\mathcal{Q}$, i.e., configurations sampled as unions of voxels Q_i it is convenient to renormalize the Minkowski functionals by setting

$$V_\nu(\mathcal{Q})=\frac{W_\nu(\mathcal{Q})}{\omega_\nu} \tag{1.4}$$

so that $V_\nu(Q_i)=1$ for a single cube (voxel) Q_i. Note that according to the definition given by Eq. (1.3) the Minkowski functionals V_ν can be considered as Euler-Poincaré characteristics χ for lower-dimensional planar intersections of the spatial configuration $\mathcal{Q}$. The Minkowski functionals in three dimensions are related to familiar geometric quantities, for instance, the surface area $6V_1$ and integral mean curvature $3\pi V_2$ of the surface exposed by a coverage with volume $\mathcal{V}=V_0$ and Euler characteristic $\mathcal{X}=V_3$.

Two general properties that a functional $\mathcal{V}(\mathcal{Q})$ should possess in order to be a morphological measure are motion invariance and continuity, since the ''shape'' of a domain does not depend on its location and orientation and should be approximately given by an inscribed polygon. In many cases it is important that a domain can be decomposed into parts such as a digitized set $\mathcal{Q}=\cup_i Q_i$ into a collection of voxels Q_i. Therefore, we require the additivity relation (1.1) as a third property of a morphological functional $\mathcal{V}(\mathcal{Q})$. Three-dimensional space examples of such measures include volume and surface area of a domain $\mathcal{Q}$. In two dimensions they include the boundary length and area. A remarkable theorem in integral geometry is the completeness of the Minkowski functionals [25]. The theorem asserts that any additive, continuous, and motion invariant functional $\mathcal{V}(\mathcal{A})$ on subsets $A\subset\mathbb{R}^d, A\in\mathcal{R}$, is a linear combination of the $d+1$ Minkowski functionals

$$\mathcal{V}(A)=\sum_{\nu=0}^{d} c_\nu V_\nu(A). \tag{1.5}$$

with real coefficients c_ν independent of A. The $d+1$ Minkowski functionals therefore are the complete set of morphological measures. The continuity of the functionals V_ν allows the definition of integrals of the curvature function to be evaluated for surfaces with singular edges, i.e., the Minkowski functionals generalize curvatures as differential geometric quantities to singular edges [12,13,16,26]. Therefore, it is straightforward to apply the notion of morphological measures even to patterns consisting of individual lattice grains (voxel-based images). Since many physical phenomena depend essentially on the geometry of spatial structures, such morphological measures may be useful tools, in particular, in combination with the Boolean model well known in stochastic geometry [13]. This model generates random structures by overlapping grains such as spheres or cubes each with arbitrary location and orientation.

The normalized mean values $v_\nu(\rho)=\langle V_\nu(\mathcal{Q})\rangle/V$ of the Minkowski functionals for Poisson-distributed lattice grains of density ρ (in units of a^{-2}, a is the lattice constant) are [13]

$$\begin{aligned} v_0(\rho)&=1-e^{-\rho V_0},\\ v_1(\rho)&=e^{-\rho V_0}(1-e^{-\rho V_1}),\\ v_2^{(8)}(\rho)&=e^{-\rho V_0}(-1+2e^{-\rho V_1}-e^{-\rho(2V_1+V_2)}),\\ v_3^{(26)}(\rho)&=e^{-\rho V_0}(1-3e^{-\rho V_1}+3e^{-\rho(2V_1+V_2)}\\ &\quad -e^{-\rho(3V_1+3V_2+V_3)}). \end{aligned} \tag{1.6}$$

where $V_\nu(K)$ are the morphological measures of the individual grains K. For Poisson-distributed cubes of sidelength λ, $\tilde{q}=1-\tilde{p}=e^{-\rho}$ being the probability that a cube is not placed at a lattice site, and $V_0=\lambda^3$, $V_1=\lambda^2$, $V_2=\lambda$, and $V_3=1$ this becomes

$$\begin{aligned} v_0(\rho)&=1-\tilde{q}^{\lambda^3},\\ v_1(\rho)&=\tilde{q}^{\lambda^3}(1-\tilde{q}^{\lambda^2}),\\ v_2^{(8)}(\rho)&=\tilde{q}^{\lambda^3}(-1+2\tilde{q}^{\lambda^2}-\tilde{q}^{2\lambda^2+\lambda}),\\ v_3^{(26)}(\rho)&=\tilde{q}^{\lambda^3}(1-3\tilde{q}^{\lambda^2}+3\tilde{q}^{2\lambda^2+\lambda}-\tilde{q}^{3\lambda^2+3\lambda+1}). \end{aligned} \tag{1.7}$$

The numbers in brackets specify the different neighborhoods of the cubes. In contrast to the measures v_0 and v_1, v_2 depends on the definition of the local neighborhood of a grain. Since one must have topological closed sets, grains may be connected only by a single point. For voxel-based images this leads to some ambiguity in the measure. On a square lattice, diagonally connected pixels have only one point in common—in the absence of a preferred continuity of either phase, the interface can be considered to be curved equally toward either medium. In the presence of strongly preferred continuity, the neighborhood will have eight neighbors (a pixel is connected to the nearest and the next-nearest neighbors) for the phase of preferred continuity and four neighbors (only nearest neighbor connections) for the other phase. This leads to a duality of these measures. Similarly on a cubic lattice one may have 6 or 26 neighbors depending on the absence or presence of preferred continuity. The continuity of either phase can be varied continuously by defining the probability α of a common edge to be continuous in one phase and the probability $\beta=1-\alpha$ in the other phase [27]. If neither phase has preferred continuity we set $\alpha=\beta=1/2$.

As shown by Seyfried and Mecke [28], one can relate the measures of $v_2(\rho)$ and $v_3(\rho)$ for different neighborhoods,

$$\begin{aligned} v_2^{(4)}(\rho)&=v_2^{(8)}(\rho)+\delta v_2,\\ v_3^{(6)}(\rho)&=v_3^{(26)}(\rho)-3\,\delta v_2+\delta v_3, \end{aligned} \tag{1.8}$$

with the two correction terms for Poisson-distributed cubes given by

$$\begin{aligned} \delta v_2&=2\tilde{q}^{\lambda^3+2\lambda^2-\lambda}(1-\tilde{q}^{\lambda})^2,\\ \delta v_3&=\tilde{q}^{\lambda^3+3\lambda^2-\lambda-1}[\tilde{q}^{4\lambda-2}(8\tilde{p}^2\tilde{q}-2)+24\tilde{q}\\ &\quad +12\tilde{q}^{3\lambda}(1+\tilde{p})-6\tilde{q}^{2\lambda}(1+4\tilde{p})+8\tilde{p}\tilde{q}^{\lambda}-24\tilde{q}^{\lambda+1}]\\ &\quad -4\tilde{q}^{\lambda^3+3\lambda^2-3\lambda+1}. \end{aligned} \tag{1.9}$$

The derivation of theoretical results for the other particle-based models is fully analogous. If spheres are used as grains, the Minkowski measures of the single grain in the continuum become

$$V_0=\frac{4}{3}\pi r^3,\quad V_1=\pi r^2,\quad V_2=2r,\quad V_3=1. \tag{1.10}$$

leading to the global measures for Poisson-distributed or identical overlapping spheres (IOS) using Eq. (1.6).

II. COMPUTATIONAL ASPECTS

In this section we describe the algorithm implemented to calculate the Minkowski functionals, the generation of the model morphologies, the validation of the algorithms on some of those model morphologies, and discretization effects.

A. Algorithm to calculate the MFs

The MFs are obtained directly from any image made up of discrete voxels. For example, the volume fraction of a phase is trivially obtained by dividing the number of voxels of that phase by the total number of voxels. The other functionals are obtained by considering the interface associated with the vertices of each voxel or the Voronoi cell of the lattice [27]. Each vertex of the lattice is shared by eight neighboring cubes; there are therefore $2^8=256$ possible configurations, which can be evaluated quickly using a masked sum

$$config=\sum_{i=0}^{7}2^i\times \mathrm{phase}_i,\quad \mathrm{phase}_i\in\{0,1\}, \tag{2.1}$$

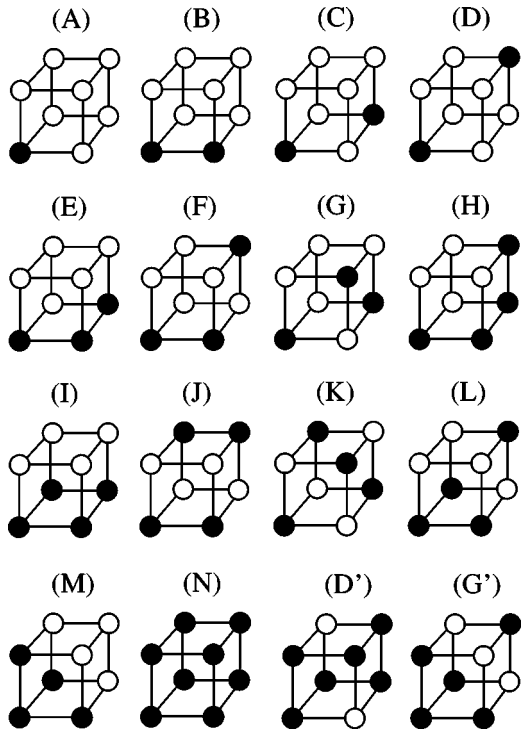

FIG. 1. Catalog of filling patterns of a unit cell giving rise to distinct configurations. Some configurations with exchanged phases are not shown; 22 isotropic configurations exist, the rest can be generated by rotations. Isotropic configurations (A)–(G) are generated by inverting the phases of configurations (A)–(G) and (N). (D') and (G') are shown as an illustration.

where the sum is taken over only one phase. For voxels of equal side length, the local Minkowski measures are rotationally invariant and the 256 configurations reduce to 22 (see Fig. 1). The mapping is given in Table I and the local contributions to the global Minkowski functionals are given in Table II. The various patterns and their resultant MFs have been derived elsewhere [27,28] for general α. The global measures for each configuration are obtained then by a configuration count over all vertices on any voxelated structure normalized by the total number of vertices. On a 500 MHz Alpha microprocessor we calculate all MFs on a 500^3 image in 40 secs using 2 MB of memory. The execution time scales linearly with the volume of the image.

B. Generation of model media

The models we considered in this paper can be loosely separated into three different classes. The first class, particle-based models, includes Poisson-distributed cubes and Poisson-distributed overlapping oblate and prolate spheroids. Cubes of slidelength $\lambda=(1,2,4,8)$ are considered. For spheroids we consider both fully oriented and isotropic packs. A special case of this model is based on overlapping spheres (IOS model). For this model we consider radii of $r=(4,8,12,16)$. Two more systems of spheroidal packs are evaluated, both with a half-axis range of $4\leqslant r\leqslant 20$ and an average half axis of $\bar{r}=12$. In one case we consider randomly oriented spheroids and in the second case spheroids fully aligned along a specific axis. Examples for some of these models are given in Fig. 2.

TABLE I. Mapping of the 256 vertex configurations to the 22 isotropic configurations following the order shown in Fig. 1. IC defines the isotropic configuration number and N the multiplicity of the configuration.

IC	N	Configuration number defined by Eq. (2.1)
0	1	0
1	8	1, 2, 4, 16, 32, 64, 128
2	12	3, 5, 10, 12, 17, 34, 48, 68, 80, 136, 160, 192
3	12	6, 9, 18, 20, 33, 40, 65, 72, 96, 130, 132, 144
4	4	24, 36, 66, 129
5	24	7, 11, 13, 14, 19, 21, 35, 42, 49, 50, 69, 76, 81, 84, 112, 138, 140, 162, 168, 176, 196, 200, 208, 224
6	24	25, 26, 28, 37, 38, 44, 52, 56, 67, 70, 74, 82, 88, 98, 100, 131, 133, 137, 145, 152, 161, 164, 193, 194
7	8	22, 41, 73, 97, 104, 134, 146, 148
8	6	15, 51, 85, 170, 204, 240
9	8	23, 43, 77, 113, 142, 178, 212, 232
10	24	27, 29, 39, 46, 53, 58, 71, 78, 92, 114, 116, 139, 141, 163, 172, 177, 184, 197, 202, 209, 216, 226, 228
11	24	30, 45, 54, 57, 75, 86, 89, 99, 101, 106, 108, 120, 135, 147, 149, 154, 156, 166, 169, 180, 198, 201, 210, 225
12	6	60, 90, 102, 153, 165, 195
13	2	105, 150
14	8	107, 109, 121, 151, 158, 182, 214, 233
15	24	61, 62, 91, 94, 103, 110, 118, 122, 124, 155, 157, 167, 173, 181, 185, 188, 199, 203, 211, 217, 218, 227, 229, 230
16	24	31, 47, 55, 59, 79, 87, 93, 115, 117, 143, 171, 174, 179, 186, 205, 206, 213, 220, 234, 236, 241, 242, 244, 248
17	4	126, 189, 219, 231
18	12	111, 123, 125, 159, 183, 190, 215, 222, 235, 237, 246, 249
19	12	63, 95, 119, 175, 187, 207, 221, 238, 243, 245, 250, 252
20	8	127, 191, 223, 239, 247, 251, 253, 254
21	1	255

A class of materials that is not in general well described by particulate models is that of amorphous composites. Recently, model random materials have been described by level cuts of a superposition of random plane waves—the leveled-wave model [29,30]. Originally developed to describe the morphologies associated with spinodal decomposition [18], and later to describe the structure of bicontinous microemulsions [19], the leveled-wave model accounts for many features observed in real disordered materials [29] including polymer blends [21] and foams [31].

In the original scheme due to Cahn [18] one associates an interface between two distinct phases (e.g., pore/matrix) with a level set (or contour) of a random standing wave $y(r)$ composed of N sinusoids with fixed wavelength $\lambda=2\pi/k_0$ but random directions $\mathbf{k}_n$, phase constants Φ_n, and amplitudes A_n,

$$y(r)=\frac{1}{\sqrt{N}}\sum_n A_n\cos(k_0\mathbf{k}_n\cdot\mathbf{r}+\Phi_r). \tag{2.2}$$

TABLE II. Local contributions to the global Minkowski measures for the 22 isotropic configurations. L gives the configuration in Fig. 1 that matches the configuration number IC.

IC	N	L	$8V_0$	$24V_1$	$24V_2^{(4)}$	$24V_2^{(8)}$	$8V_3^{(6)}$	$8V_3^{(26)}$
0	1	N'	0	0	0	0	0	0
1	8	A	1	3	3	3	1	1
2	12	B	2	4	2	2	0	0
3	12	C	2	6	6	2	2	−2
4	4	D	2	6	6	6	2	−6
5	24	E	3	5	1	1	−1	−1
6	24	F	3	7	5	1	1	−3
7	8	G	3	9	9	−3	3	−1
8	6	I	4	4	0	0	0	0
9	8	M	4	6	0	0	−2	−2
10	24	H	4	6	0	0	−2	−2
11	24	L	4	8	4	−4	0	0
12	6	J	4	8	4	−4	0	0
13	2	K	4	12	12	−12	4	4
14	8	G'	5	9	3	−9	−1	3
15	24	F'	5	7	−1	−5	−3	1
16	24	E'	5	5	−1	−1	−1	−1
17	4	D'	6	6	−6	−6	−6	2
18	12	C'	6	6	−2	−6	−2	2
19	12	B'	6	4	−2	−2	0	0
20	8	A'	7	3	−3	−3	1	1
21	1	N	8	0	0	0	0	0

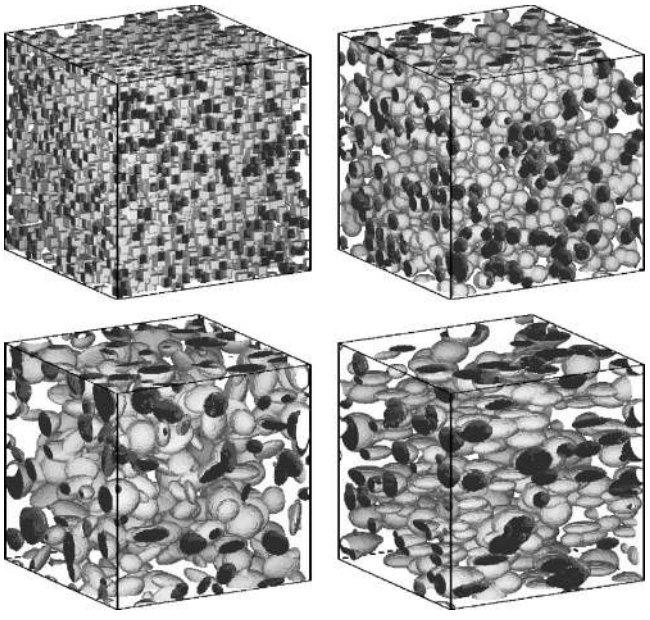

FIG. 2. The interface of models of Poisson-distributed particles. Top: cubes of sidelength $\lambda=8$ and overlapping spheres of radius $r=8$. Bottom: overlapping spheroids with a half-axis range of $r=4.20$; randomly oriented (left), fully aligned (right). The volume fraction of the particle phase is $\phi=0.25$.

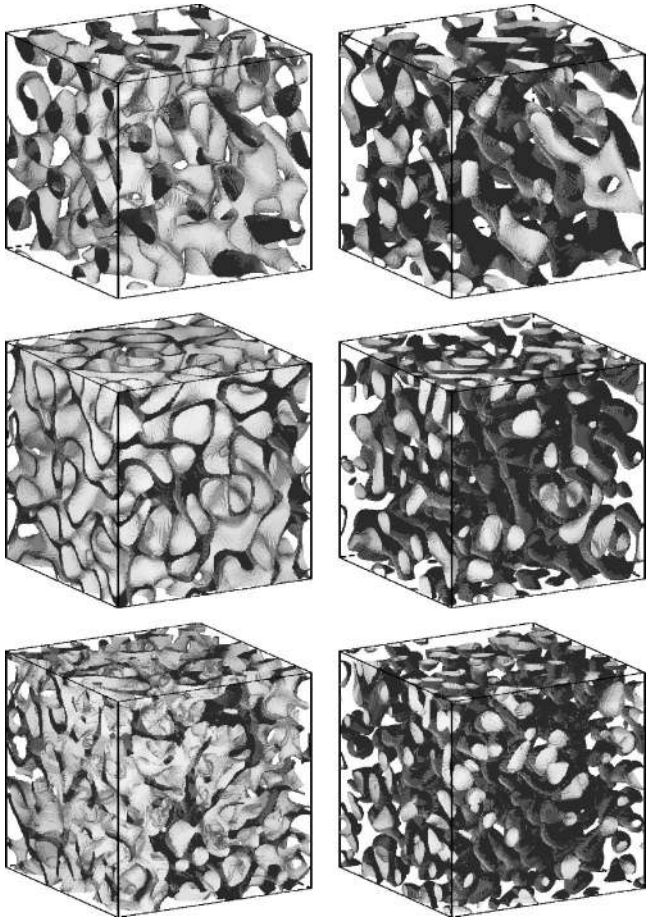

FIG. 3. The interface of Gaussian models of periodicity $t=10$ for volume fractions of $\phi=0.25$ and $\phi=0.75$ from left to right. Top, One-level cut. Middle, Two-level cut. Bottom, Intersection of two two-level cuts.

As $y(r)$ is positive as often as it is negative, a 50/50 (isometric) blend coincides with the zero set of $y(r)$. If a distribution of wavelengths is allowed, the function $y(r)$ is just a Gaussian random field (GRF). The resultant morphology is characterized by an undulating interface of consistent curvature and exhibits two similar phase structures.

Cahn's approach was extended [19] to a description of the interspace between a pair of interfaces associated with two nearby level sets of the random field. The volume between a pair of interfaces associated with two level sets of the same wave, say the level cuts $\alpha \leqslant y(r) \leqslant \beta$, is considered to be in one phase, while the two regions contiguous to this $[y(r) < \alpha; y(r) > \beta]$ are defined as a second phase. The macroscopic volume fractions of the two phases are specified once the position of the level cuts is assigned. Mathematical structures so defined exhibit a wide range of morphologies. The symmetric two-level cut mode $\alpha = -\beta$ exhibits a ribbon or sheetlike structure and is characterized by a high degree of interconnectivity (even at low volume fractions). One may choose any number of β and α for a given phase fraction ϕ. Clearly, the freedom in choosing the position of the level cuts (for a chosen volume fraction) allows one to model an even larger variety of microstructures [32].

More general models can also be developed based on this

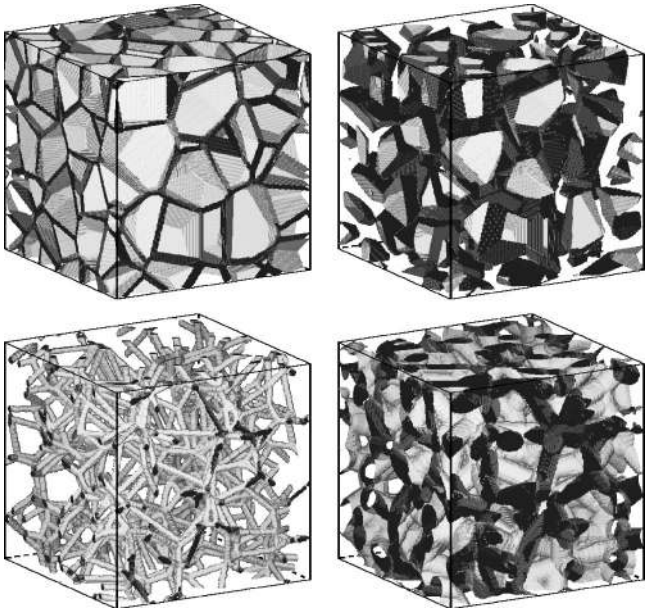

FIG. 4. The interface of Voronoi models with 100 seeds on a 200^3 lattice. First row, facet models for volume fractions of $\phi = 0.26$ (left) and $\phi = 0.74$ (right). Second row, edge models for volume fractions of $\phi = 0.06$ (left) and $\phi = 0.50$ (right).

approach. Intersection sets of any number of fields can be generated [33,34]. In this paper we consider the intersection of two two-level cut fields that are thought to accurately describe the pore morphologies of sandstones [35]. Realizations of each of the Gaussian models are shown in Fig. 3.

The third class of morphologies, random cellular solids [24], are constructed using a Voronoi tesselation. In this model we subdivide space randomly into convex polyhedra by scattering Poisson points to a given density and construct the bisecting plane between each pair of points. From the tiles formed by the intersections of the bisecting planes between a given Poisson point and its neighbor, we construct convex polyhedra. Within each polyhedra every point is closer to the given Poisson point than to any other. The resultant structure is similar to that of a closed-cell foam or random honeycomb. By thickening the walls of the polyhedra we probe a large range of phase fractions. To do this we generate a Euclidean distance map (EDM)—a mapping giving the Euclidean distance (1, $\sqrt{2}$, $\sqrt{3}$, 2, ...) of each voxel from its nearest surface voxel. By stepping through the different distances a range of phase fractions for the morphology is generated.

To form a foamlike network of low coordination number we considered the trisecting planes of the Poisson points. By using the EDM we grow a network of connected cylinders. At fractions below ca. 10% this may be a good model of foams (see, e.g., Figs. 2 and 4 in [36]) and of aerogels [34]. Examples of the Voronoi structures are given in Fig. 4.

C. Validation of the algorithm

The algorithm for calculating the Minkowski measures was validated against theoretical predictions for model systems of Poisson-distributed cubes of equal sidelength (Fig. 2)

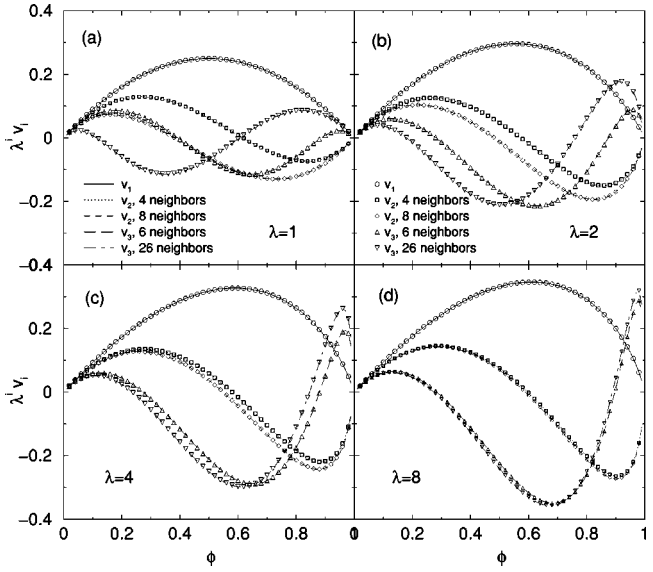

FIG. 5. Minkowski measures over fraction: comparison of theoretical predictions (lines) with numerical simulations (symbols) for Poisson-distributed cubes at different sizes: (a) $\lambda = 1$, (b) $\lambda = 2$, (c) $\lambda = 4$, and (d) $\lambda = 8$. The measures are scaled as $v_1 \rightarrow \lambda v_1$, $v_2 \rightarrow \lambda^2 v_2$, and $v_3 \rightarrow \lambda^3 v_3$.

given by Eqs. (1.7)–(1.9) as well as Poisson-distributed spheres of identical radius. All computational data are based on a minimum of 50 realizations on a 200^3 lattice. We measure the MFs over the full range of the volume fraction ϕ in steps of $\Delta\phi = 0.02$ for each model. The models are mapped periodically, therefore, edge effects can be ignored.

As can be seen in Fig. 5 the numerical data matches the theoretical [Eqs. (1.7)–(1.9)] prediction for cubes of varying sidelength. For cubes with $\lambda = 1$ the result reduces to random filled lattices as simulated by Jernot and Jouannot [17].

To match the predictions for spheres, one must be careful with the definition of the local measures of each spherical grain. One must use the local Minkowski measures of the digital sphere and not a continuum sphere of equivalent radius [using Eq. (1.10) directly]. We define the digital sphere of radius r by all voxels radiating from the central voxel that are separated by a euclidean distance $\ell < r$. The discretized one-dimensional radius for continuum spheres is given by $r_{1d} = r_c - 0.5$ because the spheres are centered at a vertex. The properties of the discretized sphere are given in Table III. Using these values for the local measures in Eqs. (1.7)–

TABLE III. Comparison of the local Minkowski measures in two and three dimensions for spherical grains in the continuum against the discretized spheres used in the simulations. We use* to denote the continuum values as compared to the discretized. V_1 is given by $V_1 = 2r_1$.

r_*	V_2^*	V_2	V_3^*	V_3	r_1	r_2	r_3
4	50.3	45	268.1	251	3.5	3.79	3.91
8	201	193	2145	2103	7.5	7.84	7.95
12	452	437	7238	7141	11.5	11.8	12.0
16	804	793	17157	17071	15.5	15.9	16.0

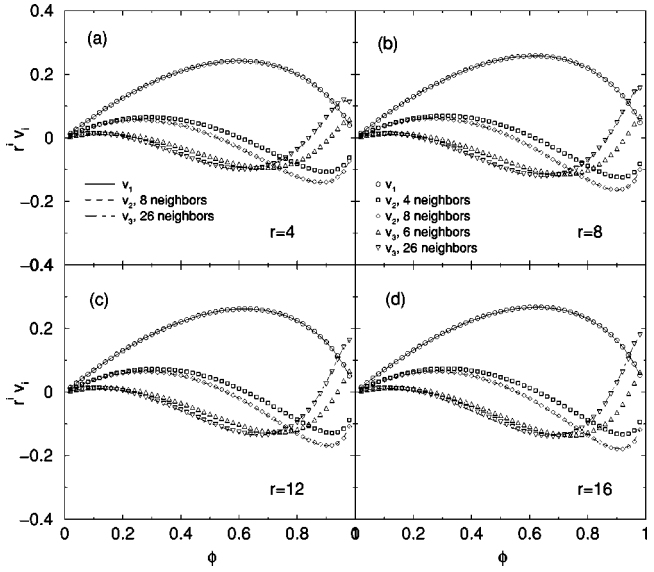

FIG. 6. Minkowski measures over fraction: comparison of theoretical predictions (lines, highly connected neighborhoods) with numerical simulations (symbols, both neighborhoods) for Poisson-distributed spheres of different radius: (a) $r=4$, (b) $r=8$, (c) $r=12$, and (d) $r=16$. The measures are scaled as $v_1 \rightarrow r v_1$, $v_2 \rightarrow r^2 v_2$, and $v_3 \rightarrow r^3 v_3$.

(1.9) we obtain excellent agreement with theory (see Fig. 6).

The symmetry of the Euler characteristic for dimensions $d>1$ was also checked. Interchanging phases correctly mirrors

$$v_2^{(4)}(\phi) \rightarrow -v_2^{(8)}(1-\phi),$$
$$v_3^{(6)}(\phi) \rightarrow v_3^{(26)}(1-\phi) \tag{2.3}$$

for all binary models.

D. Discretization effects

Here we discuss the effect of the choice of preferred continuity on the measure of the MFs. In particular, we consider the effect on the Euler characteristic. In Table I of [27] and Table IX of [28] the local contribution to the Euler characteristic in three dimensions of the 22 possible local configurations of the unit cell is described. The eight (ambiguous) configurations that are dependent on preferred continuity are configurations *C, D, F, G*, C', D', F', and G' of Fig. 1. To consider the discretization effects in the measure of the Euler characteristic, we compare the contribution of these configurations to both Poisson-distributed cubes at different λ and to the IOS model at different r (see Fig. 7). One observes that for the Poisson cube model, the contributions are only considerable for $\lambda=2$ and 4, while for larger λ the effects are minimal. This is mirrored in Fig. 5, where we observed the convergence of the curves for 6 (26) neighborhoods for large λ. The reason for the fast convergence of the different neighborhoods is that, configurations giving rise to the ambiguous configurations only occur for cubes that are exactly adjacent. *Any* overlap of two adjacent cube surfaces will eliminate the possibility of generating these configurations. Thus we find that the contribution of these configurations scales approximately as the cube volume l^{-3} over most of the fractional range. For the IOS model the contributions do decrease, but more slowly, as r^{-1}. The contribution of these configurations to models exhibiting large local curvature is considerable even at higher resolutions. The choice of preferred continuity should be considered carefully for boolean models with curved surfaces.

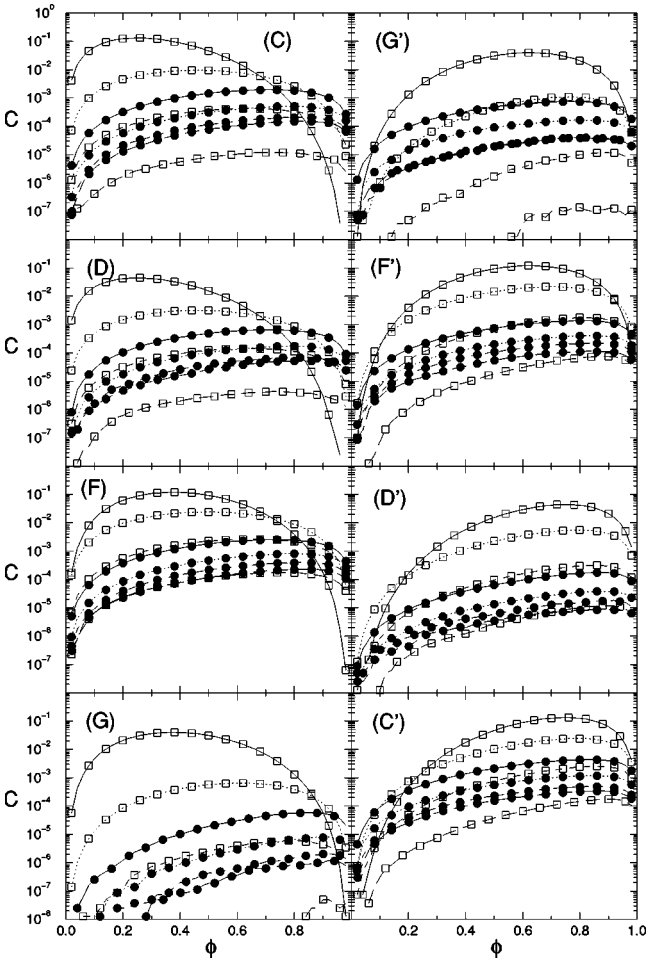

FIG. 7. The configuration probabilities $C=C(X)$ over fraction of Poisson-distributed cubes and spheres for the ambiguous configurations (X) in Fig. 1. The letters correspond to the specific configurations. Data for the cube model is given by open squares and for the IOS by solid circles. The configurational probabilities decrease with increasing size. Here we show data for sphere radii, $r=(4,8,12,16)$, and for the cube sidelength, $l=(1,2,4,8)$.

III. RESULTS

In this section we report and discuss the Minkowski functionals of the different microstructures and qualitatively compare between the models. We generate the model microstructures at *roughly* the same length scales.

The MFs are in general size dependent. For example, the Euler characteristic per unit volume for a sphere pack of radius $r=4$ cannot be directly compared to results for a sphere pack of radius $r=16$. A dimensionless measure such

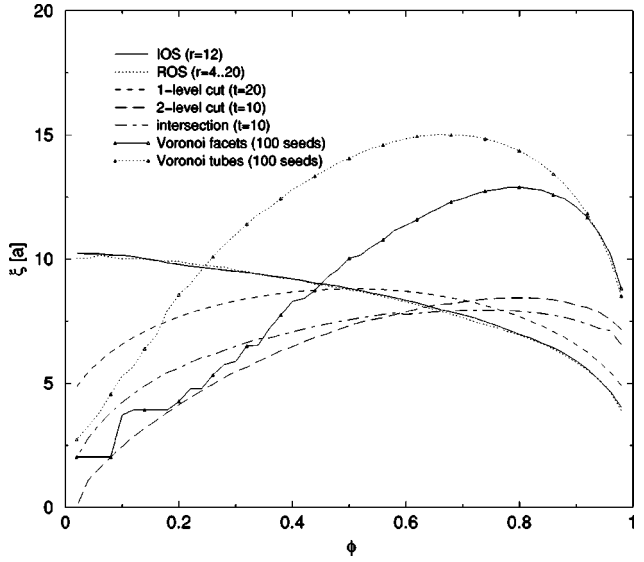

FIG. 8. Correlation length over fraction derived from the two-point correlation functions in real space in units of the lattice constant a; IOS, identical overlapping spheres; ROS, randomly oriented spheroids; three different Gaussian and two Voronoi tesselation models.

as the Euler characteristic per particle would be of great use in comparing results. In Fig. 6 we showed the MFs for the IOS model at different radii. By scaling the measures $v_1 \rightarrow r v_1$, $v_2 \rightarrow r^2 v_2$, and $v_3 \rightarrow r^3 v_3$, we see approximate overlap of the curves, therefore, scaling of this particulate model by particle size is appropriate.

However for general models the definition of a particle size is problematic. For example, the one- and two-level cut Gaussian models generated from the same field exhibit very different correlation functions, the correlation function for the two-level cut model decaying far more rapidly than in the single-level cut case. This point is observed by visual inspection of Fig. 3. We therefore choose our model systems to have similar correlation lengths ξ defined by the decay of the envelope of the spatial two-point correlation function. In some cases, for example the two-level cut Gaussian, the correlation length at low volume fractions is very small, so direct comparison is difficult. In Fig. 8 we plot the correlation length ξ for the range of models considered in this paper for different volume fractions. The choice of the periodicity T for the Gaussian fields and the density of sites for the Voronoi models were made to closely match the particle-based models for $r=12$ across the range of volume fraction ϕ. This allows us to form a basis for a semiquantitative comparison of the MFs across the range of models.

A. Comparison of MFs for different model morphologies

1. Particle-based models

First we discuss the MFs for particle-based models shown in Figs. 5 and 6. Other than the discretization effects discussed above, there is little difference when comparing the data for Poisson-distributed cubes and spheres. For cubes of sidelength $l=1$ the measures show a higher symmetry; Eq. (1.8) is satisfied without interchanging phases.

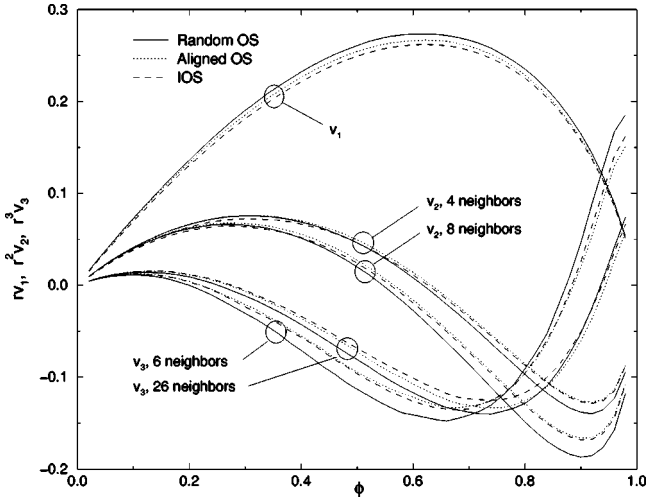

FIG. 9. Minkowski measures over fraction for Poisson-distributed overlapping spheroids of half axes $r=4.20$, with $\bar{r}=12$, compared to fully aligned overlapping spheroids of the same size distribution and IOS of $r=12$. The measures are scaled as $v_1 \rightarrow \bar{r} v_1$, $v_2 \rightarrow \bar{r}^2 v_2$, and $v_3 \rightarrow \bar{r}^3 v_3$.

We compare the sensitivity of the Minkowski measures to deviations in form or alignment. To do this we consider packs of overlapping spheroids. We generate randomly oriented and fully aligned overlapping spheroids of uniformly distributed half axes $r=4,...,20$ and $\bar{r}=12$ and compare them to the IOS model with $r=12$. As Fig. 9 shows, the Minkowski measures for these systems are quite similar. In fact, the different continuity rules have a far stronger effect than the differences in size or alignment. It may be nontrivial to distinguish the measures for these different systems.

2. Gaussian models

The Gaussian one-level cut model results in symmetric MFs around $\phi=0.5$ (see Fig. 10). The integral mean curvature is much less than for the particle-based models. For small and large ϕ, isolated elliptical inclusions are present

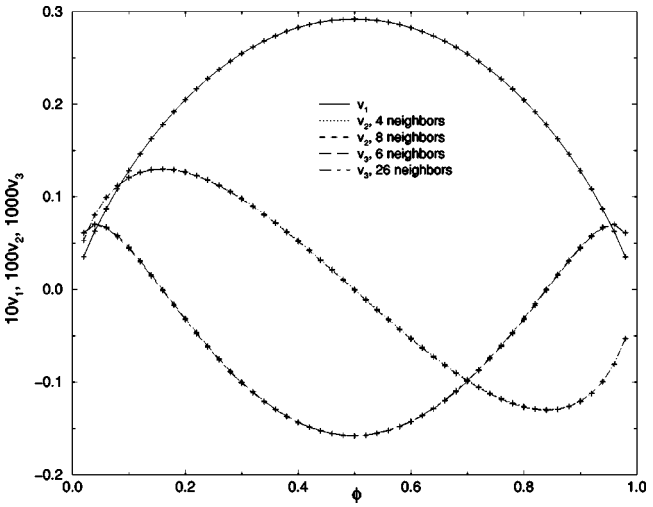

FIG. 10. Minkowski measures over fraction for Gaussian one-level cut models of periodicity $t=20$.

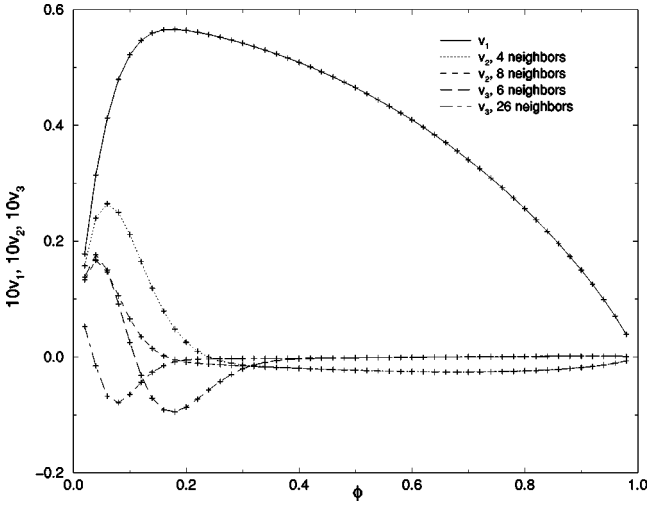

FIG. 11. Minkowski measures over fraction for Gaussian two-level cut models of periodicity $t=20$.

and the Euler characteristic is positive. In the regime $\phi \simeq 0.20-0.80$, the interface becomes predominantly hyperbolic ($v_3<0$) and both phases are continuous. The relative smoothness (small local curvature) of the interface when compared to the sphere pack model leads to a low probability for obtaining ambiguous configurations. Accordingly the measures for the two different neighborhoods converge.

For the symmetric two-level cut Gaussians of small ϕ the surface to volume ratio is much larger than for the previous systems. Particularly, at low volume fractions the morphology exhibits a sheetlike phase and the surface to volume ratio quickly reaches a maximum (Fig. 11). Further densification is associated with a thickening of the sheets and the surface to volume ratio drops. Also for small ϕ, discretization effects are important and the different neighborhoods play an important role. The Euler characteristic is very large and becomes negative for small ϕ once the sheetlike phase connects implying a strongly bicontinuous structure, as is evident in Fig. 3.

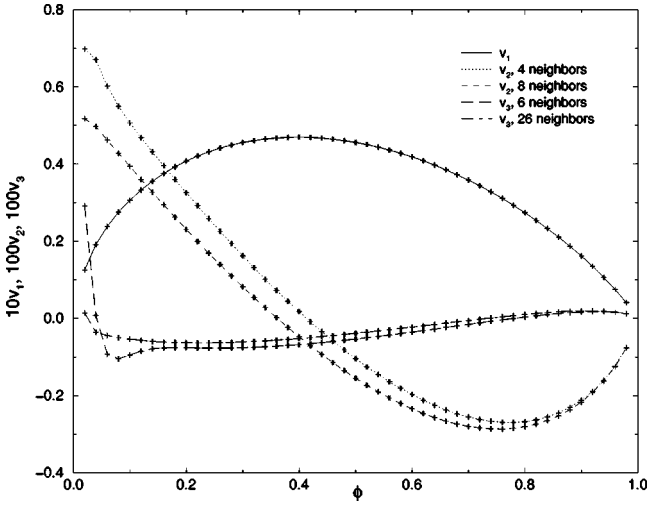

FIG. 12. Minkowski measures over fraction for Gaussian intersection models of periodicity $t=20$.

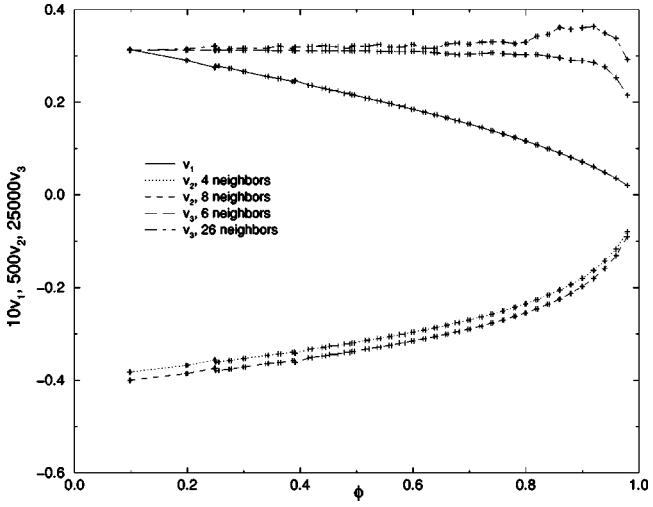

FIG. 13. Minkowski measures over fraction for Voronoi facet models of 100 seeds on a 200^3 lattice.

The intersection set of the two two-level cut Gaussians has a distinct signature (Fig. 12) when compared to the one- and two-level cut models. The strong Gaussian curvature feature at small ϕ may be useful as a signature of this structure when compared with the other models.

3. Voronoi models

For the Voronoi facet model, the connected polyhedra phase always percolates, and the other phase is made up of disconnected inclusions. Accordingly, the curvature never changes sign—the holes remain convex for all ϕ (Fig. 13). Similarly, the Euler characteristic always remains positive, while the surface area due to the construction of the fields starts at a maximum and decreases with thickening facet boundaries. Small ambiguities arise at the intersections of the facets, again giving rise to a separation of the MFs based on the choice of continuity.

For the Voronoi cylinder model, both the network of cylinders and the background phase percolate over a wide range

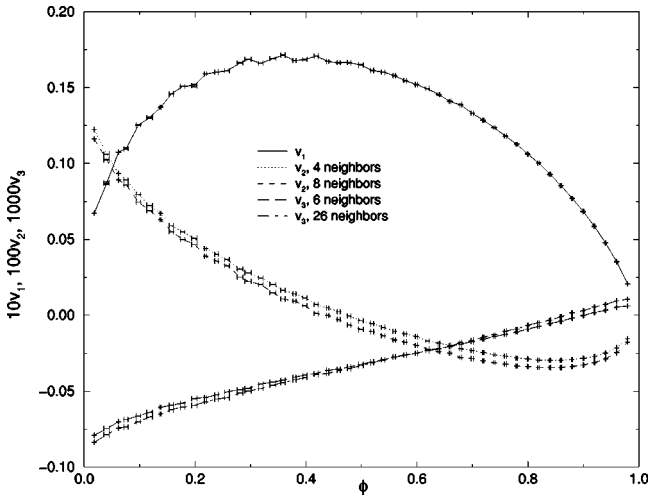

FIG. 14. Minkowski measures over fraction for Voronoi edge models of 100 seeds on a 200^3 lattice.

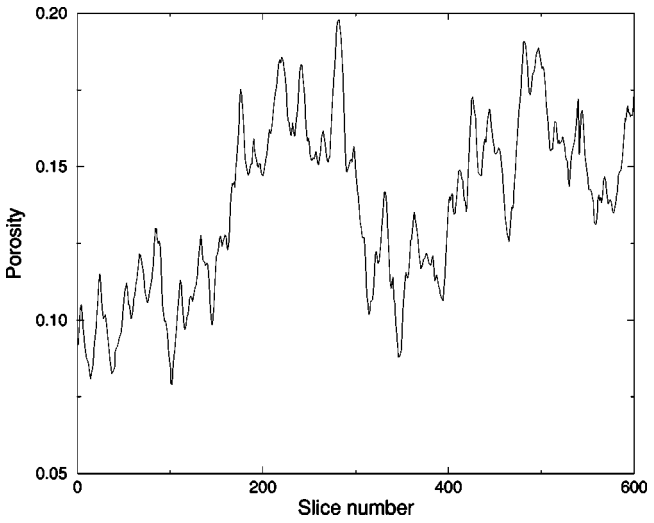

FIG. 15. Variation in the porosity distribution along a cross-bedded sandstone sample.

of ϕ. Here, the surface area first grows with increasing cylinder radius and then decreases again after the cylinders begin merging (Fig. 14). The curvature decreases with increasing dilation and becomes negative once individual edges of the Voronoi cells begin to generate isolated inclusions of the background phase. The Euler characteristic is initially negative, implying that both phases percolate, and then increases almost linearly, finally becoming positive.

IV. CALCULATION OF CHARACTERISTICS ON A SANDSTONE SAMPLE

Direct measurement of a three-dimensional structure is now available via micro x-ray computed microtomography micro-CT [37–39]. These techniques provide the opportunity to experimentally measure the complex morphology of a range of materials in three dimensions at resolutions down to 5 μm. We have obtained a $512\times512\times666$ image of a cross-bedded sandstone at 10 μm resolution via micro-CT imaging. Analysis of the full image would give us a single value for each of the MFs and would give us little data to compare model predictions. However, this sample shows strong heterogeneity in the pore volume fraction. We show in Fig. 15 a trace of 600 values of the porosity measured at a separation of 10 μm. Due to this heterogeneity and by appropriately choosing different window sizes on the image we are able to generate morphological parameters for the sandstone for a range of ϕ. This allows us to quantitatively compare the experimental microstructure for different proposed model morphologies.

The original sample view was of a cylindrical plug with 512×512 voxels in the plane and 660 slices. Two cubic blocks of $300\times300\times300$, 16 blocks of $150\times150\times150$, 54 blocks of $100\times100\times100$, and 250 blocks of $60\times60\times60$ were obtained from the full sample volume. This provided a spread of porosities across different sampling volumes (see Fig. 16). Results for the morphological measures are summarized in Fig. 17. With decreasing sampling volume the variability of the measures increases, but the values are consistent with the data for the larger volumes, suggesting that for the smaller blocks a meaningful average is obtained.

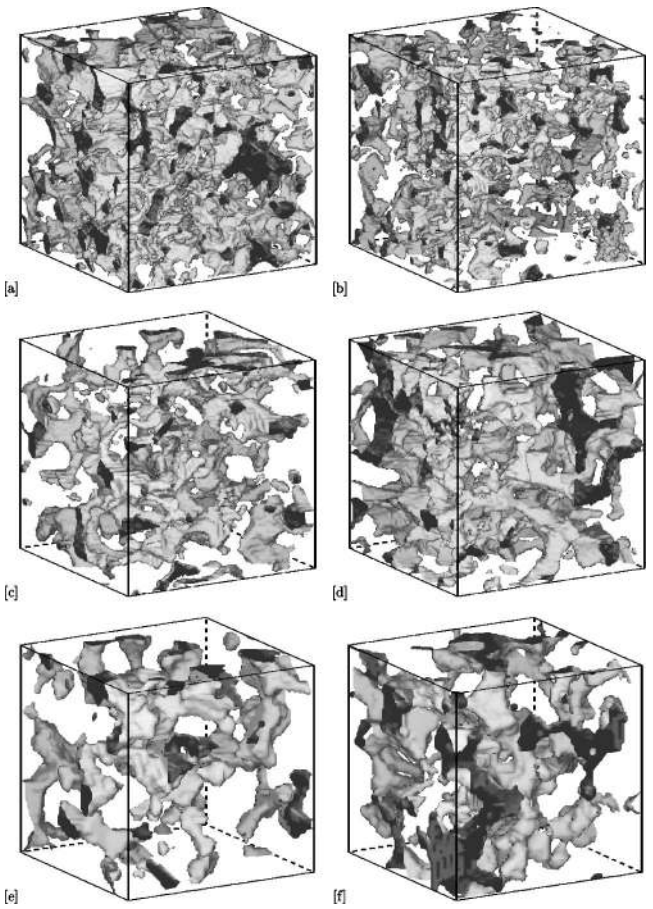

FIG. 16. The pore structure for sections of the x-ray-CT data of the cross-bedded sandstone for different window sizes. (a), (b) 150^3, (c), (d) 100^3, (e), (f) 60^3. The spread in ϕ is evident across the samples.

A number of statistical models have been proposed for reconstructing porous media from statistical information [1,2,33,35,40–42]. These methods, based on different underlying model microstructures, are generated in such a manner that they match the observed two-point statistical properties of the rock. We compare the morphological measures for the sandstone to three standard stochastic models used to generate realizations of sedimentary rock microstructures from two-point information [43]. The first is based on the boolean sphere model [41], the second on the one-level cut model [1,2], and the third on the intersection set model [35]. The quantities used to characterize the microstructures of these systems are the volume fraction, the surface to volume ratio s/v, and $p^{(2)}(r)$ the two-point correlation function. Note that $\phi=p^{(2)}(0)$ and $s/v=-4dp^{(2)}(0)/dr$.

The correlation function for the phase external to the spheres of radius r_0 in the IOS model is $p^{(2)}(r)=p^{(\nu(r))}$ for $r<2r_0$ and $p^{(2)}(r)=\phi^2$ for $r>2r_0$, where $\nu(r)=1+3r/4r_0-r^3/16r_0^3$, and $s/v=-3\phi\ln\phi/r_0$. To generate matching GRF models we employ the field-field correlation function [44,33]

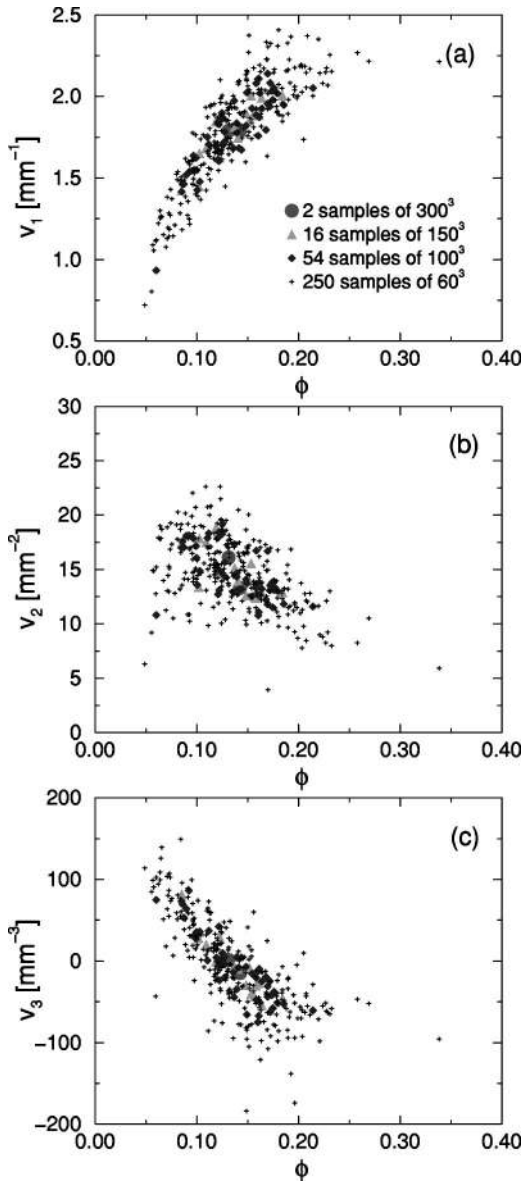

FIG. 17. Minkowski measures for a cross-bedded sandstone. Shown are the data points for the different blocks of sizes 60^3, 100^3, 150^3, and 300^3. In this case the measures are plotted over porosity, not over fractions of a constituting grain density. From top to bottom: (a) v_1, (b), $v_2^{(8)}$, and (c) $v_3^{(26)}$.

$$g(r)=\frac{e^{-r/\xi}-(r_c/\xi)e^{-r/r_c}}{1-(r_c/\xi)}\,\frac{\sin 2\pi r/d}{2\pi r/d} \tag{4.1}$$

characterized by a correlation length ξ, domain scale d, and a cutoff scale r_c. The three length scale parameters are obtained by a best fit procedure to minimize the nonlinear least squares error [33],

$$Ep^{(2)}=\frac{\sum_{i=1}^{M}[p_{\rm fit}^{(2)}(r_i)-p_{\rm exp}^{(2)}(r_i)]^2}{\sum_{i=1}^{M}[p_{\rm fit}^{(2)}(r_i)-p_{\rm exp}^2]^2}, \tag{4.2}$$

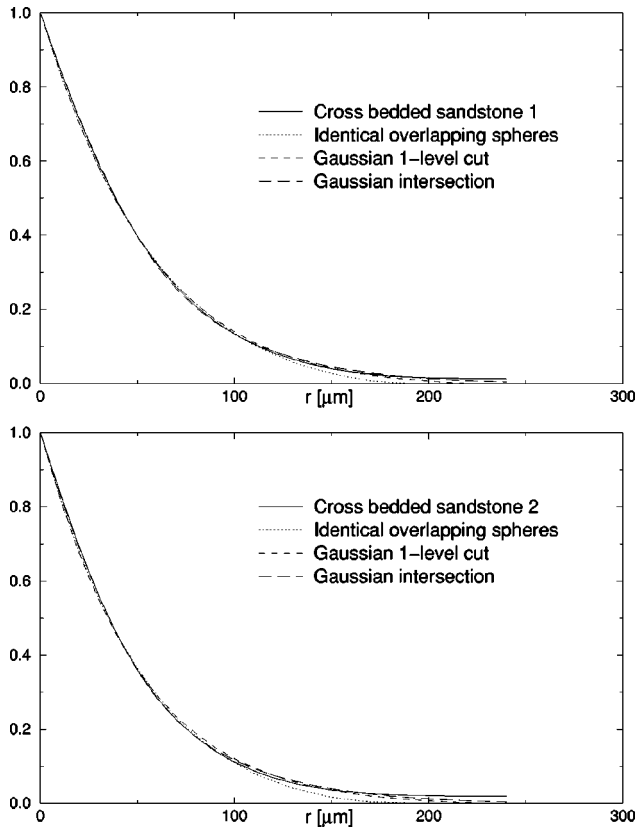

FIG. 18. Normalized two-point correlation functions $S(r)$ of the two 300^3 sandstone samples and the averaged best fits for the model structures.

and a downhill simplex method is used to find the best parameter set [45]. We generate the stochastic models that best match the two $300\times300\times300$ samples and compare the normalized two-point correlation functions $S(r)=[p_2(r)-p^2]/(p-p^2)$ of these models in Fig. 18.

Values of r_0 for the IOS model, and d, ξ, and r_c are summarized in Table IV along with the error estimate $E(p^{(2)})$. The average fit is worst for the sphere model, and more than a factor of 2 better for the Gaussian one-level cut and intersection set. The sphere model, however, has only one free parameter as compared to three for the Gaussian models.

We then calculate the Minkowski functionals of the three stochastic models and compare them with the sandstone data (Fig. 19). The measures are compared to the values resulting from the sampling window at 100^3. The values for the samples were binned in steps of porosity $\Delta\phi=0.02$.

TABLE IV. Parameters of the models for the cross-bedded sandstone in microns. The original sandstone data set image has resolution at 10 μm per pixel. For the IOS model, the equivalent sphere radius is in the r_c column.

Model	r_c (μm)	ξ (μm)	d (μm)	$Ep^{(2)}$
Spheres	94.2			2×10^{-3}
One-level cut	20.2	22.4	1080	9×10^{-6}
Intersection	54.3	80.5	410	4×10^{-4}

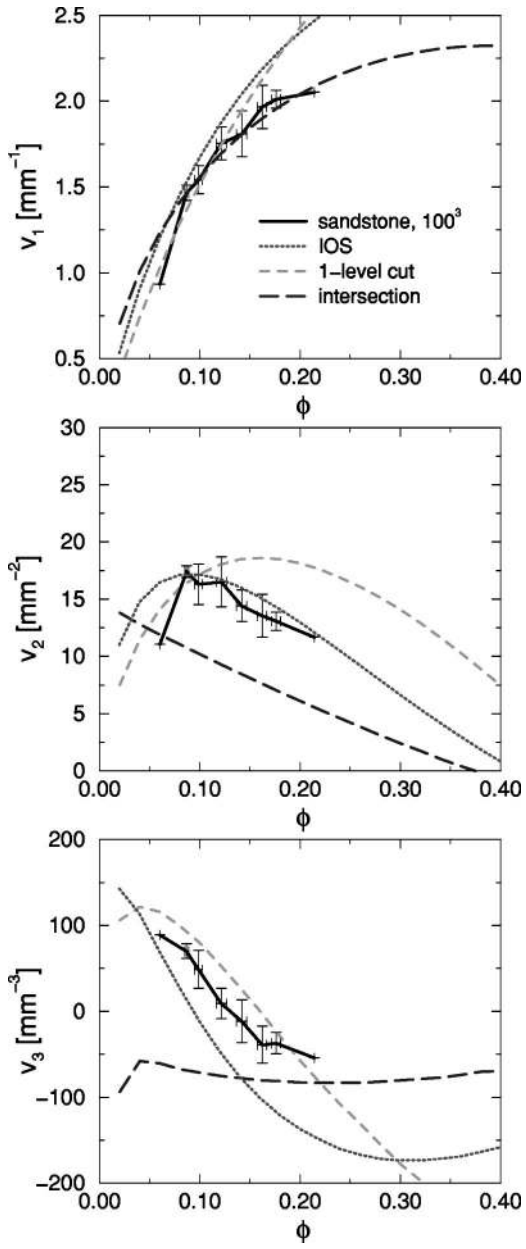

FIG. 19. Comparison of the MFs for the sandstone data to the three stochastic models based on a window size of 100^3.

None of the models satisfactorily match the experimental data. The surface area v_1 is matched best across all ϕ by the intersection model. Integral curvature v_2 is best matched by the IOS models that honor the granularity of the sedimentary rock. The topology v_3 is described well by both the IOS and the one-cut models. The intersection model is particularly poor for this model over the full range of ϕ. The model that best captures the characteristics of the sandstone is the IOS model. Even though the other models do reasonably well at the fraction where the two-point correlation functions were matched, they fail to describe the structure across a range of phase fractions. Different transport and mechanical processes will depend more strongly on the agreement with *specific* morphological measures. For example, single phase flow and conductivity will be most strongly affected by surface-to-volume (related to average constriction size) and the topology. A model that accurately describes these measures may still yield good agreement with experiment. However, multiphase flow properties depend crucially on the curvature of the surfaces where immiscible phases meet. For these processes a model that also accurately matches v_2 will be required. In this case the IOS model is the best of the three candidates as a reconstructed data set. Recently, a model for describing sandstone morphology has been developed based on a full process-based sedimentation, compaction, and diagenesis model [46]. This model honors both the shape of the original grains and the geological formation processes and therefore may provide a more accurate description of pore space morphology of sedimentary rock.

V. CONCLUSIONS

Integral geometry provides alternative methods and tools for measuring spatial structure. A family of measures, the Minkowski functionals (MFs), in particular, seem to be promising measures for describing the morphology of complex materials. The MFs characterize not only the connectivity but also the shape and content of spatial figures. These measures embody information from every order of the correlation function but can be calculated simply by summing over local contributions of a configuration. In three dimensions the functionals are related to the familiar measures of volume fraction, surface area, integral mean curvature, and Euler characteristic. The morphological measures are useful order parameters for describing spatial patterns quantitatively and providing for a comparison between experiment and theory.

They may also play a role in the statistical reconstruction of complex three-dimensional morphologies. To date, methods used to reconstruct morphologies have been primarily based on averaged statistical pointwise information to second order. In previous simulated annealing procedures the energy function has been defined by the ''distance'' from the reference two-point correlation function [47] and the chord distribution function [6]. After interchanging voxels on a digitized representation, one must perform a *nontrivial* calculation of two-point information on the new structure to decide if the move is accepted or rejected. Integral geometry provides an alternative method to measure spatial structure, and use of the measures may lead to fast simulated annealing procedures for reconstructing random media. In contrast to the methods based on two-point information, the interchange of voxels leads to local changes in the MFs, and trial states are more easily evaluated.

ACKNOWLEDGMENTS

M.A.K. thanks the Australian Research Council for financial support. K.R.M. acknowledges support from Deutsche Forschungsgemeinschaft (DFG Grant No. Me1361/7). We thank the A.N.U. Supercomputing Facility for generous allocations of computer time. The CT image of the sandstone was obtained by Richard Ketcham at the High Resolution CT facility at the University of Texas.

[1] M. Joshi, Ph.D. thesis, University of Kansas, Lawrence, 1974.
[2] P. Adler, C. Jacquin, and J.-F. Thovert, Water Resour. Res. **28**, 1571 (1992).
[3] J. Fredrich, K. Greaves, and J. Martin, Int. J. Rock Mech. Min. Sci. Geomech. Abstr. **30**, 691 (1993).
[4] *Image Analysis and Mathematical Morphology*, edited by J. Serra (Academic Press, New York, 1992), Vol. 2.
[5] N. Roberts, M. Reed, and G. Nesbitt, J. Microsc. **187**, 110 (1997).
[6] C. L. Y. Yeong and S. Torquato, Phys. Rev. E **57**, 495 (1998).
[7] A. Scheidegger, *The Physics of Flow through Porous Media* (University of Toronto Press, Toronto, 1974).
[8] C. Manwart, S. Torquato, and R. Hilfer, Phys. Rev. E **62**, 893 (2000).
[9] R. Hilfer, *Advances in Chemical Physics* (Wiley, New York, 1996), Vol. 92, pp. 299–424.
[10] A. Rosenfeld, *Digital Picture Processing* (Academic Press, New York, 1976).
[11] L. A. Santaló, *Integral Geometry and Geometric Probability* (Addison-Wesley, Reading, MA, 1976).
[12] K. Mecke, Acta Phys. Pol. B **28**, 1747 (1997).
[13] *Statistical Physics—The Art of Analyzing and Modeling Spatial Structures*, edited by K. R. Mecke and D. Stoyan, Lecture Notes in Physics (Springer-Verlag, Berlin, 2000), Vol. 554.
[14] K. R. Mecke, Phys. Rev. E **53**, 4794 (1996).
[15] K. Jacobs, S. Herminghaus, and K. R. Mecke, Langmuir **14**, 965 (1998).
[16] K. R. Mecke, in *Integralgeometric in der Statistischen Physik: Perkolation, Komplexe Flüssigkeiten und die Struktur des Universums* (Harry Deutsch, Frankfurt, 1994), pp. 61–68.
[17] J. P. Jernot and P. Jouannot, J. Microsc. **171**, 233 (1993).
[18] J. W. Cahn, J. Chem. Phys. **42**, 93 (1965).
[19] N. F. Berk, Phys. Rev. Lett. **58**, 2718 (1987).
[20] P. Pieruschka and S. Marčelja, Langmuir **10**, 345 (1994).
[21] M. A. Knackstedt and A. P. Roberts, Macromolecules **29**, 1369 (1996).
[22] H. Jinnai *et al.*, Phys. Rev. Lett. **78**, 2248 (1997).
[23] C. H. Arns, M. A. Knackstedt, W. V. Pinczewski, and A. P. Roberts, Macromolecules **32**, 5964 (1999).
[24] L. Gibson and M. Ashby, *Cellular Solids: Structure and Properties* (Pergamon, Oxford, 1988).
[25] H. Hadwiger, *Vorlesungen über Inhalt, Oberfläche und Isoperimetrie* (Springer, Berlin, 1957).
[26] K. R. Mecke, Int. J. Mod. Phys. B **12**, 861 (1998).
[27] S. T. Hyde, I. S. Barnes, and B. W. Ninham, Langmuir **6**, 1055 (1990).
[28] A. Seyfried and K. R. Mecke (unpublished).
[29] N. F. Berk, Phys. Rev. A **44**, 5069 (1991).
[30] M. Teubner, Europhys. Lett. **14**, 403 (1991).
[31] A. P. Roberts and M. Knackstedt, J. Mater. Sci. Lett. **14**, 1357 (1995).
[32] A. P. Roberts and M. Knackstedt, Phys. Rev. E **54**, 2313 (1996).
[33] A. P. Roberts, Phys. Rev. E **56**, 3203 (1997).
[34] A. P. Roberts, Phys. Rev. E **55**, R1286 (1997).
[35] A. P. Roberts, D. P. Bentz, and M. Knackstedt, in Society of Petroleum Engineers Paper No. 37024, 1996 (unpublished).
[36] C. Monnereau and M. Vignes-Adler, J. Colloid Interface Sci. **202**, 45 (1998).
[37] B. P. Flannery, H. W. Deckman, W. G. Roberge, and K. L. D'Amico, Science **237**, 1439 (1987).
[38] J. H. Dunsmuir, S. R. Ferguson, and K. L. D'Amico, in *Conference on Photoelectric Imaging Devices*, IOP Conf. Proc. No. 121 (Institute of Physics, London, 1991), p. 257.
[39] P. Spanne *et al.*, Phys. Rev. Lett. **73**, 2001 (1994).
[40] J. Quiblier, J. Colloid Interface Sci. **98**, 84 (1984).
[41] P. zen Wong, J. Koplik, and J. P. Tomanic, Phys. Rev. B **30**, 6606 (1984).
[42] S. Bryant, D. Mellor, and C. Cade, AIChE J. **39**, 387 (1993).
[43] One can derive more complex model systems that incorporate other two-point correlation information (e.g., chord distribution functions [5,4]). Recent work [8] has shown that these measures give a poor representation of connectivity. Preliminary results on MFs of these more complex models indicate that this is reflected in a poor match to the v_2 measure.
[44] M. Teubner and R. Strey, J. Chem. Phys. **87**, 3195 (1987).
[45] J. A. Nelder and R. Mead, Comput. J. (UK) **7**, 308 (1965).
[46] P. Oren, S. Bakke, and O. J. Arntzen, SPE J. **3**, 324 (1998).
[47] M. D. Rintoul and S. Torquato, J. Colloid Interface Sci. **186**, 467 (1997).